A Population-Based Atlas of the Macroscale Structural Connectome in the Human Brain

Fang-Cheng Yeh[1,2,*], Sandip Panesar[1], David Fernandes[1], Antonio Meola[3], Masanori Yoshino[4], Juan C Fernandez-Miranda[1], Jean M. Vettel[5,6,7], and Timothy Verstynen[8,*]

[1]Department of Neurological Surgery, University of Pittsburgh Medical Center, Pittsburgh, Pennsylvania, USA

[2]Department of Bioengineering, University of Pittsburgh, Pittsburgh, Pennsylvania, USA

[3]Rose Ella Burkhardt Brain Tumor and Neuro-Oncology Center, Cleveland Clinic, Cleveland, Ohio, USA

[4]Department of Neurosurgery, Toranomon Hospital, Tokyo, Japan

[5]U.S. Army Research Laboratory, Aberdeen Proving Ground, Aberdeen, Maryland, USA.

[6]Department of Psychological and Brain Sciences, University of California, Santa Barbara, Santa Barbara, California, USA.

[7]University of Pennsylvania, Department of Bioengineering, Philadelphia, PA, USA
[8]Department of Psychology and Center for the Neural Basis of Cognition, Carnegie Mellon University, Pennsylvania, USA.

*Correspondence to:

Fang-Cheng Yeh, M.D. Ph.D.
Department of Neurological Surgery,
University of Pittsburgh, Pittsburgh, Pennsylvania
Email: frank.yeh@pitt.edu

Timothy D. Verstynen Ph.D.
Department of Psychology and Center for the Neural Basis of Computation,
Carnegie Mellon University
Pittsburgh, PA, USA
Email: timothyv@andrew.cmu.edu

Key words: structural connectome, tractography atlas, connectogram, diffusion MRI

Abstract

A comprehensive map of the structural connectome in the human brain has been a coveted resource for understanding how brain networks function under normal and pathological conditions. Here we report an expert-vetted, population-based atlas of the structural connectome derived from diffusion MRI data (N=842). This was achieved by creating a high-resolution template of diffusion patterns averaged across individual subjects and using tractography to generate 550,000 trajectories of representative white matter fascicles. The trajectories were clustered and labeled by a team of experienced neuroanatomists. Multi-level network topology was illustrated by connectograms of the whole brain, subdivisions in the association, projection, and commissural pathways, and individual fiber bundles. This atlas of the structural connectome represents normative neuroanatomical organization of human brain white matter, complimentary to traditional histologically-derived and voxel-based white matter atlases, allowing for better modeling and simulation of brain connectivity for future connectomic studies as well as clinical and educational applications.

Introduction

The organization of structural connectivity in the human brain determines how neural networks communicate, thereby serving as a critical constraint on brain functionality and providing potential etiology for clinical pathology [1, 2]. Characterizing this structural organization has relied on either histological slides or neuroanatomically-validated atlases based on individual subjects [3, 4]; however, a population-based 3-dimensional (3D) structural connectome at the macroscale level has yet to be constructed. A population-based connectome is critical for demonstrating representative topological interconnectivity in the general population, a stated objective of the national investment in the Human Connectome Project [5, 6]. If achieved, such a map of the structural connectome could augment existing histological and single-subject atlases, thus allowing for robust modeling and simulation in both empirical and theoretical studies.

To date, diffusion MRI is the only non-invasive tool for mapping the 3D trajectories of human macroscopic white matter pathways [7, 8]. This is realized by resolving local fiber orientations at the voxel level and delineating entire axonal trajectories by implementing a stepwise tracking algorithm [9]. Nonetheless, caveats of diffusion MRI fiber tracking include false tracts and suboptimal white matter coverage [10, 11]. The validity of tractography can range from 3.75% to 92% due to differences in reconstruction methods and algorithms [12]. An optimized tracking approach is required for achieving the highest validity. To further reduce false fibers, image acquisition should utilize a contemporary high-angular-resolution modality [13], and any collection of tracked pathways should undergo examination by expert neuroanatomists.

Here we constructed a population-based structural connectome by a template-based and expert-vetted approach. We employed high-angular-resolution diffusion MRI data (n=842) from healthy subjects in the Human Connectome Project (HCP) database [14] and aggregated them into an averaged template of

diffusion distributions that can inform the orientations of underlying fiber architectures. The averaged diffusion pattern of the entire sample is thus representative of normative, non-pathological structural characteristics within healthy subjects. Based on this template, a total of 550,000 tracks (density around 1 track per voxel) were generated using a tracking method that was shown to achieve the highest number of valid connections in an open competition [12]. Generated tracks were subsequently clustered and then labeled by a team of clinical neuroanatomists, capitalizing on their previous experience in both cadaveric white-matter and comparative tractography techniques [15, 16]. Furthermore, the tracks were categorized into the projection, association, commissural, cerebellar, brainstem, and cranial nerve pathways to generate multi-level connectograms illustrating network topology at the macroscopic level. The strategy of this approach allowed us to compile a comprehensive atlas of the structural connectome in the human brain at the population level, allowing for taxonomical identification of pathways that together comprise the full macroscopic structural connectome.

Results

A high spatial and angular resolution diffusion template of the human brain

Diffusion MRI data from 842 participants was reconstructed in a standard space to calculate the spin distribution function (SDF)[17, 18] within each voxel (Fig. 1a). An SDF is an empirical distribution of the density of diffusing water orientations, calculated for each voxel to reveal the underlying fiber architectures (Fig. 2a). The SDFs of all subjects were averaged to build an SDF template, heretofore called the HCP-842, which represents an average diffusion pattern within a normal population (Fig. 1b). As shown in Fig. 2, the magnitude of the peaks (Fig. 2b) and their orientations (Fig. 2c) derived from the SDF template reliably reflect the coverage of white matter structures and inform their local fiber orientations (red: left-right, green: anterior-posterior, blue: inferior-superior). The peaks on an SDF suggest the local orientations of underlying fiber bundles, whereas the magnitudes measured at the

peaks provide quantitative measurements for connectivity. These offer the necessary information for a fiber-tracking algorithm to delineate long-distance white matter trajectories.

Qualitatively, the HCP-842 appears to resolve underlying neuroanatomical architecture with high fidelity: Comparing a coronal slice of the HCP-842 (1-mm resolution, Fig. 2d) with a similar section from the BigBrain histology image (the 200-micron resolution version, Fig. 2e), we see that HCP-842 clearly delineates subcortical structures such as the hippocampus (HIP), substantia nigra (SN), red nucleus (RN), and thalamus (TH). The high spatial resolution of the orientation map is even more apparent at the anterior commissure (AC) (Fig. 2f), a small left-right connecting pathway clamped by the pre-commissural (PreC) and post-commissural (PostC) branches of fornix that run in the vertical direction (color-coded by blue). The clamping structure formed between AC and fornix is a benchmark for examining the spatial resolution of the template. Fig. 2f resolves AC from the PreC and PostC branches, whereas Fig. 2g shows the averaged SDFs at the same region depicting the structural characteristics of AC with the PreC and PostC branches of the fornix. The ability to resolve branches of fornix from AC reveals the intricate sensitivity of the HCP-842 to map detailed brain connections.

Supervised labeling and segmentation of major pathways

We applied whole-brain fiber tracking to the HCP-842, producing a total of 550,000 fiber trajectories in the standard space to achieve an average density of 1 track per voxel (Fig. 1c). A white matter mask was used to remove tracks that have premature terminations in the core white matter. The remaining whole-brain tracks were then automatically clustered by a single-linkage clustering algorithm, generating unique clusters of fiber bundles (Fig. 1d). The trajectories that were proximally close to one another were grouped. Each cluster could subsequently contain a different number of trajectories based on the anatomical proximity of the tracks. Suppl. Fig. S1 shows the largest 40 clusters as an example. A team of clinical neuroanatomists examined and labeled the clusters according to neuroanatomical

nomenclature. Suppl. Table S1 lists all labels used in naming the clusters and the relevant neuroanatomy literature used for examination. Label "X" indicates a false tract, which may arise due to false continuations (Suppl. Fig. S2a) or premature termination (Suppl. Fig. S2b). Only the 550 largest clusters were used because the false rate (either false continuation or premature termination) increased substantially in clusters with a smaller size (Suppl. Fig. S2c).

The labeled clusters were subsequently merged according to their neuroanatomy label, and missing components of the large fiber bundles were tracked separately and merged to ensure completeness as per the literature (Fig. 1e). The high-angular-resolution can be appreciated in the corticospinal tracts generated from HCP842 (Suppl. Fig. S3a), showing a fanning projection pathway from the precentral (motor) cortex. By contrast, prior voxel-based white matter atlases (http://www.natbrainlab.co.uk/atlas-maps) based on lower angular acquisition scans only show the main trunk of the pathway (Suppl. Fig. S3b), as the anatomical evidence (Suppl. Fig. S3c, modified from Gray's Anatomy) indicates its missing lateral parts.

A population-based atlas of macroscopic structural connectome

The full atlas of the structural connectome is shown in Fig. 3 (abbreviation listed in Suppl. Table S1) and includes the most comprehensive map of white matter pathways yet reported. This includes the projection pathways that connect cortical areas with subcortical nuclei, brain stem nuclei, and brainstem. Acoustic radiation has not been previously reported in tractography due to the complicated crossing pattern involved with the pathway. The association pathways connect disparate cortical areas, including a set of U-fibers (U) which have not previously been comprehensively tracked or presented in the standard space. The commissural pathways connect the two hemispheres and include the corpus callosum, anterior commissure, and posterior commissure. The cerebellar pathways include the cerebellar tracts (CB) and peduncles (SCP, MCP, ICP), and they provide the major input, output, and

internal connectivity of the cerebellum. We were even able to resolve several brainstem pathways, such as central tegmental tract (CTT), dorsal longitudinal fasciculus (DLF), lateral lemniscus (LL). Finally, we discovered a limit of the current spatial resolution, where a set of cranial nerves including CN III, CN VII, and CN VIII were successfully identified, but CN I, IV, VI, and IX could not be identified due to insufficient spatial resolution. The detailed connective routes of the structural connectome atlas are presented in Supporting Information, including projection pathways (Suppl. Fig. S4), association pathways (Suppl. Fig. S5), commissural pathways (Suppl. Fig. S6), cerebellar pathways (Suppl. Fig. S7), brainstem pathways (Suppl. Fig. S8), and cranial nerves (Suppl. Fig. S9). The atlas data, including the track trajectories and connectograms, are available at http://brain.labsolver.org.

Neuroanatomical constraints on connective topology

The atlas of the structural connectome from the HCP-842 addresses a critical need in connectivity estimates that suffer from a high false positive error rate [11, 12]: the atlas enables estimation of normative region-to-region connectivity that is anatomically constrained. Figure 4 shows region-to-region connectivity matrix weighted by the SDF magnitude along the fiber pathways, segmented into the projection, association, and commissural pathways. The abbreviations for brain region are listed in Suppl. Table S2. Higher intensity (white) indicates greater SDF magnitude along the pathway. This anatomically-constrained view of structural connectivity between gray matter targets highlights how specific classes of white matter pathways define unique connective topologies. For example, commissural pathways have a generally symmetrical topology of connections between the hemispheres, with greater homotopic connectivity than heterotopic connectivity, whereas the association pathways are more uniform in their intra-cortical connections.

Finally, the connectograms of the structural connectome are illustrated in a multi-level approach (Fig. 5). The connectogram of the whole brain pathways illustrates the first level of the gross network topology

(Fig. 5a, the high-resolution version shown in Suppl. Fig. S10). The overall figure shows a dense network topology, and its network characteristics cannot be readily visualized due to the high complexity of the brain network at this level. The connectograms of the projection, association, and commissural pathways in Fig. 5b, 5c, and 5d depict the second level of the network topology (high-resolution details in Suppl. Fig. S11), and within this level, the connectograms start to reveal important network features. The projection pathway in Fig. 5b indicates hub structures at thalamus, putamen, and brainstem, illustrating the role of these regions in integrative sensorimotor function between the cerebral cortex and corresponding peripheral systems. The association pathway, as shown in Fig. 5c, forms clusters within each hemisphere and contributes a substantial amount of clustering coefficient and local efficiency (Fig. 6), elucidating its small-worldness that involves multiple relevant gray matter regions. The commissural pathways, as shown in Fig. 5d, serve as a bridge connecting both hemispheres and provide global efficiency (Fig. 6) to integrate information across cerebral hemispheres. In Fig. 5e, the connectograms of each fiber bundle are further divided to show the third level of the network topology in much more detail, and the illustration reveals a consistent hub formation for different fiber bundles, albeit with an alternative connectivity pattern to the cerebral cortex. Fig. 5f also shows clustering topology within different cortical areas, whereas Fig. 5g shows bridge-like structures. Together, these unique topologies based on the class of fiber pathway highlights the rich taxonomy of structural connectome in the human brain that reflects unique information processing constraints.

Discussion

Having an accurate, high-resolution and normative map of both the trajectories of macroscopic white matter pathways and their connectivity diagram has remained an unmet challenge in human neuroscience. Here we present the first complete atlas of the structural connectome that delineates fiber pathways within the cerebrum, cerebellum, brainstem, and a subset of cranial nerves. The fiber

trajectories were generated from a group-averaged template of 842 subjects using a fiber tracking algorithm that has been shown to minimize tracking errors relative to other methods [19]. Using an automated clustering approach, tracks were grouped into small bundles and subsequently labeled by a team of clinical neuroanatomists and vetted according to their neuroanatomic nomenclature. This combination of optimizing strategies allowed us to construct a high-quality, group-averaged structural connectome atlas of the human brain, and this HCP-842 atlas and it associated data set will be made publicly available (http://brain.labsolver.org) to promote future connectomic studies and assist neuroscientists to gain insight into the structural topology of the human brain.

We should note that several white matter atlases have been released before, and these mainly consisted of voxel segmentation on individual subjects labeling the core of major pathways using a low angular resolution approach [20-23]. Several tractography atlases [24-27] were also developed using diffusion tensor imaging [28], which was known to have lower angular resolution and cannot resolve crossing patterns [29, 30]. Our atlas, by contrast, is the first population-based atlas from 842 individuals using high angular and high spatial resolution data, allowing for the resolution of multiple fiber populations within a white matter region to delineate the intertwining architecture of human white matter. The population-based map of the structural connectome reflects both the 3D trajectories of white matter fascicles and delineates *how* gray matter regions are physically connected. This comprehensive atlas covers all white matter regions within the cerebrum, cerebellum, and brainstem. The atlas offers structural detail of both large and small pathways, including the clamping structure between the fornix and the anterior commissure, which cannot be discerned from individual studies due to lower resolution and signal-to-noise ratio of conventional diffusion MRI.

While overcoming many challenges, our current approach still has its limitations. Several cranial nerves that are smaller than 1-mm resolution were missed. These can only be tracked using images acquired at

a much higher resolution. In addition, the expert examination may have its own errors, especially for identifying minor pathways and branches. It is also possible that the branching patterns of the white matter pathways differ person from person. Unfortunately, the representative pathways provided by our population-based atlas cannot address individual differences. Finally, the atlas reveals only three levels of the network topology, as more recent studies have focused on subcomponents of the fiber bundles (e.g. SLF I, II, and III)[15, 16]. Although the spatial resolution of the atlas can be improved, it provides a macroscopic framework for future connectomic studies to explore microscopic connections under its categorical system.

Despite these limitations, a vetted atlas of the structural connectome has many benefits for clinical, scientific, and educational applications. It can be used to confirm or explore potential cortical connections, and the atlas can be used to derive a normative pattern of network measures to assist graph theoretical analysis of clusters and hubs in the brain connectome. In cognitive neuroscience, the atlas can augment functional-structural correlative inferences. In clinical research, the 3D trajectories of major fiber pathways can aid researchers in localizing white matter structures of interest (e.g., electrode placement during deep brain stimulation surgery). Such investigators can use this atlas as an interactive roadmap as they evaluate individual-subject connectomic data. This, for example, may enable future investigations into the correlation of white-matter lesions with known gross-white matter structures. Another advantage of the current atlas is that it includes a normative template of diffusion distribution across the brain. This may allow for future efforts comparing normal diffusion patterns with those from the neurological or psychiatric pathologies. Finally, in science education, the atlas is a novel resource superseding conventional 2D slice-based histological atlases. The trajectory information provides panoramic views on the relative location of each white matter bundle, allowing for an in-depth understanding of the white matter structure.

Online Methods

Diffusion MRI acquisitions

We used the preprocessed data from Human Connectome Projects (Q4 release, 2015) acquired by Washington University in Saint Louis and University of Minnesota. A total of 842 subjects (372 males and 470 females, age 22 ~ 36) had diffusion MRI scanned on a Siemens 3T Skyra scanner using a 2D spin-echo single-shot multiband EPI sequence with a multi-band factor of 3 and monopolar gradient pulse. The spatial resolution was 1.25 mm isotropic. TR=5500 ms, TE=89.50 ms. The b-values were 1000, 2000, and 3000 s/mm^2. The total number of diffusion sampling directions was 90, 90, and 90 for each of the shells in addition to 6 b0 images. The preprocessed data were corrected for eddy current and susceptibility artifact. The matrices for gradient nonlinearity distortion correction were used in the following diffusion MRI reconstruction.

Super-resolution q-space diffeomorphic reconstruction

The diffusion data were reconstructed in the ICBM-152 space (ICBM: International Consortium for Brain Mapping) using the q-space diffeomorphic reconstruction (QSDR)[18], a method that conserved the diffusible spins after nonlinear transformation and could be applied to DTI, DSI, and multishell data. QSDR calculated the spin distribution function (SDF), $\psi(\hat{\mathbf{u}})$, an orientation distribution function defined as the density of spins that have diffusion displacement oriented at direction $\hat{\mathbf{u}}$ during the diffusion time:

$$\psi(\hat{\mathbf{u}}) = \left| J_\varphi \right| Z_0 \sum_i W_i(\varphi(\mathbf{r})) \mathrm{sinc}\left(\sigma\sqrt{6Db_i} < \hat{\mathbf{g}}_i, \frac{J_\varphi \hat{\mathbf{u}}}{\left\| J_\varphi \hat{\mathbf{u}} \right\|} > \right) \qquad (1)$$

Where φ is a diffeomorphic mapping function that maps standard space coordinates $\mathbf{r}$ to the subject's space. J_φ is the Jacobian matrix of the mapping function, whereas $\left| J_\varphi \right|$ is the Jacobian determinant. $W_i(\varphi(\mathbf{r}))$ are the diffusion signals acquired at $\varphi(\mathbf{r})$. b_i is the b-value, and $\hat{\mathbf{g}}_i$ is the direction of the diffusion sensitization gradient. σ is the diffusion sampling ratio controlling the detection range of the diffusing spins. D is the diffusivity of water, and Z_0 is the constant estimated by the diffusion signals of free water diffusion in the brain ventricle [18]. The nonlinearity of diffusion gradients was corrected using the nonlinear terms of the magnetic field obtained from gradient coils. The HCP dataset includes a 3-by-3 gradient deviation matrix for each voxel to estimate the effective gradient direction and strength. This matrix was applied to the diffusion sensitization gradient, $\hat{\mathbf{g}}_i$ in Eq. (1) to correct the effect of gradient nonlinearity.

To achieve super-resolution reconstruction, we modified a nonlinear registration algorithm that used Fourier basis as the deformation function [31] to boost the registration accuracy. The original setting used a set of 7-by-9-by-7 Fourier basis at x-y-z directions for 2-mm resolution, and the computation and memory bottleneck was at the inverse step of a 1327-by-1327 matrix (not a sparse matrix). We increased the resolution of the Fourier basis by 4-fold to 0.5-mm resolution (i.e. 28-by-36-by-28 Fourier basis), which required solving an 84676-by-84676 matrix for each optimization iteration.

Here instead of solving the large matrix using a standard Gauss-Jordan method (a complexity of $O(n^3)$), which would increase the computation time by a factor of $(4\times4\times4)^3=262,144$, we used the Jacobi method that allowed for parallel processing and could utilize solutions from the previous iteration to speed up the processing. This greatly reduced the computation complexity to $O(n)$ and only increased the computation time by a factor of $4\times4\times4=64$. The parallel processing further reduced the computation time, allowing us to reconstruct the data using multi-thread resources. The registration accuracy was

evaluated by the R-squared value between the subject and template image. This goodness-of-fit value allowed us to identify two problematic datasets (#173132 and #103515) and reported them to the HCP consortium (https://www.mail-archive.com/hcp-users@humanconnectome.org/msg01939.html).

Construction of an SDF template

The q-space diffeomorphic reconstruction was conducted for all subjects to compute the SDFs. The SDFs of all subjects were then averaged, voxel-by-voxel, to obtain an SDF template, termed HCP-842. The computation was conducted using the cluster at Center for the Neural Basis of Cognition, a joint Institute of Carnegie Mellon University and the University of Pittsburgh. The cluster had 24 nodes and 320 CPUs. The 842 subjects took a month of computation time to complete.

Whole-brain tractography

We used a deterministic fiber tracking algorithm that used the SDF information to achieve higher accuracy [32]. Each of the tracks generated was automatically screened for its termination location. A white matter mask created by 0.6 Otsu's threshold was used to eliminate tracks with premature termination in the white matter region. The total number of tracks was set to achieve an average seeding density around 1 track per voxel. Specifically, the fiber tracking was conducted using angular thresholds of 40, 50, 60, 70, and 80 degrees. Each angular threshold generated 100,000 tracks, and a total of 500,000 tracks were obtained. Since the white matter mask also removed tracks connecting to/from the spinal cord, an additional set of whole brain tracking was conducted to allow tracks terminates at the lowest section of the brainstem. The fiber tracking was also conducted using angular thresholds of 40, 50, 60, 70, and 80 degrees. Each angular threshold generated 10,000 tracks, and a total of 50,000 tracks were obtained.

Initial clustering using Hausdorff distance

We compared the clustering results for middle frontal gyrus streamlines from two subjects to the output of single linkage hierarchical clustering and K-means clustering. For single linkage clustering, we measured the Hausdorff distance between a pair of fibers X and Y as

$$d_H(X, Y) = \max\{ \max_{x \in X} \min_{y \in Y} d(x, y), \max_{y \in Y} \min_{x \in X} d(x, y) \}$$

X is a set of coordinates, i.e. X={x}, whereas Y is another set of coordinates, i.e. Y={y}. d(x,y) calculates the Euclidian distance between two coordinates x and y, and the $d_H(X,Y)$ calculates the Hausdorff distance between set X and Y. The first set of whole brain tracks was clustered using 2 mm as the single linkage threshold, and we only selected 500 largest clusters because the rest of smaller clusters contained less than 0.01% of the total tracks (i.e. < 50 tracks). This selection was further justified in our expert examination, in which we found that the probability of a smaller cluster being recognized as false tracks was higher (Fig. 4c). The same cluster selection strategy was applied to our second set of the tracks (i.e. the tracks connecting to/from spinal cords). A single linkage clustering was conducted using 2 mm as the threshold, and the first 50 largest clusters were collected. The resulting clusters contain unique trajectories without repeated tracks, and the largest 550 clusters were selected whereas the other smaller clusters were discarded. Since each cluster may contain tracks with repeated trajectories, we removed redundant trajectories that are substantially close to the one another using a Hausdorff distance of 1mm.

Expert labeling and examination

The 550 clusters were manually labeled by our neuroanatomy teams, including three senior neuroanatomists (JFM, AM, MY, FY) and junior neuroanatomists (DF and SP). The labeling was based

on evidence from publicly available white matter atlases, existing literature, microdissection evidence, and neuroanatomy books (Table S1). The first examination round is the manual labeling conducted by 3 neuroanatomists (FY, DF, and SP). Each of the neuroanatomists independently labeled each of the 550 clusters. Inter-observer differences were identified, including the naming of the cluster and whether the cluster is a false or real. The differences were resolved in a joint discussion (FY, DF, SP, and JFM). The clusters with the same neuroanatomy name were grouped together to form major fiber bundles. The merged bundles underwent a second round of inspection by both senior and junior neuroanatomists to identify missing branches and remove false connections. The inspection identified missing branches in anterior commissure (olfactory and occipital connections), corticothalamic tract (temporal connections), corticostriatal tract (occipital connections), corticospinal tracts (lateral), corticopontine tracts (temporal and occipital connections), and corpus callosum (the tapetum). These branches were specifically tracked by a region-based approach by placing regions of interest at the target area. The final fiber bundles were subsequently categorized into the projection, association, commissural, cerebellar, brainstem, and cranial nerve pathways.

The next examination round further checked for other missing minor pathways that require a dense sampling to form a bundle. This was done by projecting the fiber bundles back to the white matter and looking for areas without track coverage. Using a region-based approach, the senior neuroanatomists (MY, AM, and FY) tracked missing minor pathways including acoustic radiation, posterior commissure, brainstem pathways such as RST, STT, DLF, LL, ML, and cranial nerves such as CNVII, CNVIII, and CNX. These pathways were tracked according to previous microdissection studies [15, 16]. Due to the limitation of fiber tracking, the course of the posterior column sensory pathway, running within the fascicles gracile and cuneatus toward the primary sensory cortex, was manually terminated at the level

of the thalamus and labeled as medial lemniscus (ML). This segment in the brainstem corresponds to the second order neurons running from the nucleus gracile and cuneatus to the thalamus.

Connectivity matrix, connectogram, and network measures

A weighted connectivity matrix was quantified using a cortical parcellation was based on regions derived from the AAL atlas (Table S2). It is noteworthy that our tractography atlas can be readily applied to any cortical parcellation atlas, and currently there is no consensus on how network nodes should be defined. Here we used only one of the most popular parcellation from the AAL atlas to illustrate the network characteristics.

The average of along-track SDF values was used as the connectivity value. The connectograms of each fiber bundle and whole brain tracks were generated using CIRCOS (http://mkweb.bcgsc.ca/tableviewer/visualize/). The network measures such as network characteristic path length, global efficiency, local efficiency, clustering coefficient were calculated using the definition formulated in Brain Connectivity Toolbox (https://sites.google.com/site/bctnet/). The influence of the projection, association, and commissural pathways was calculated by calculating the change of network measures (quantified by percentage of the original) after removing the tracks.

Resources

The processing pipeline (DSI Studio), SDF data of all 842 subjects, and HCP-842 template are available at http://dsi-studio.labsolver.org. The SDF template can be reproduced using the HCP data and documentations on the website. The atlas data, including the track trajectories and connectograms, are available at http://brain.labsolver.org.

Acknowledgements

References

1.   Sporns, O. Contributions and challenges for network models in cognitive neuroscience. *Nat Neurosci* **17**, 652-660 (2014).

2.   Bota, M., Sporns, O. & Swanson, L.W. Architecture of the cerebral cortical association connectome underlying cognition. *Proc Natl Acad Sci U S A* **112**, E2093-2101 (2015).

3.   Amunts, K. et al. BigBrain: an ultrahigh-resolution 3D human brain model. *Science* **340**, 1472-1475 (2013).

4.   Ding, S.L. et al. Comprehensive cellular-resolution atlas of the adult human brain. *J Comp Neurol* **524**, 3127-3481 (2016).

5.   Setsompop, K. et al. Pushing the limits of in vivo diffusion MRI for the Human Connectome Project. *Neuroimage* **80**, 220-233 (2013).

6.   Van Essen, D.C. et al. The WU-Minn Human Connectome Project: an overview. *Neuroimage* **80**, 62-79 (2013).

7.   Fan, Q. et al. MGH-USC Human Connectome Project datasets with ultra-high b-value diffusion MRI. *Neuroimage* **124**, 1108-1114 (2016).

8.   McNab, J.A. et al. The Human Connectome Project and beyond: initial applications of 300 mT/m gradients. *Neuroimage* **80**, 234-245 (2013).

9.   Wedeen, V.J. et al. The geometric structure of the brain fiber pathways. *Science* **335**, 1628-1634 (2012).

10.   Reveley, C. et al. Superficial white matter fiber systems impede detection of long-range cortical connections in diffusion MR tractography. *Proc Natl Acad Sci U S A* **112**, E2820-2828 (2015).

11.   Thomas, C. et al. Anatomical accuracy of brain connections derived from diffusion MRI tractography is inherently limited. *Proc Natl Acad Sci U S A* **111**, 16574-16579 (2014).

12.   Maier-Hein, K. et al. Tractography-based connectomes are dominated by false-positive connections. *bioRxiv* (2016).

13.   Glasser, M.F. et al. The Human Connectome Project's neuroimaging approach. *Nat Neurosci* **19**, 1175-1187 (2016).

14.   Van Essen, D.C. et al. The Human Connectome Project: a data acquisition perspective. *Neuroimage* **62**, 2222-2231 (2012).

15.   Wang, X. et al. Subcomponents and connectivity of the superior longitudinal fasciculus in the human brain. *Brain Struct Funct* **221**, 2075-2092 (2016).

16.   Fernandez-Miranda, J.C. et al. Asymmetry, connectivity, and segmentation of the arcuate fascicle in the human brain. *Brain Struct Funct* **220**, 1665-1680 (2015).

17.   Yeh, F.C., Wedeen, V.J. & Tseng, W.Y. Generalized q-sampling imaging. *IEEE Trans Med Imaging* **29**, 1626-1635 (2010).

18. Yeh, F.C. & Tseng, W.Y. NTU-90: a high angular resolution brain atlas constructed by q-space diffeomorphic reconstruction. *Neuroimage* **58**, 91-99 (2011).

19. Maier-Hein, K., Neher, P., Houde, J. C., Cote, M. A., Garyfallidis, E., Zhong, J., ... & Reddick, W. E. Tractography-based connectomes are dominated by false-positive connections. *bioRxiv* **084137** (2016).

20. Zhang, S., Peng, H., Dawe, R.J. & Arfanakis, K. Enhanced ICBM diffusion tensor template of the human brain. *Neuroimage* **54**, 974-984 (2011).

21. Peng, H. et al. Development of a human brain diffusion tensor template. *Neuroimage* (2009).

22. Mori, S. et al. Stereotaxic white matter atlas based on diffusion tensor imaging in an ICBM template. *Neuroimage* **40**, 570-582 (2008).

23. Mori, S., Oishi, K. & Faria, A.V. White matter atlases based on diffusion tensor imaging. *Curr Opin Neurol* **22**, 362-369 (2009).

24. Zhang, W., Olivi, A., Hertig, S.J., van Zijl, P. & Mori, S. Automated fiber tracking of human brain white matter using diffusion tensor imaging. *Neuroimage* **42**, 771-777 (2008).

25. Guevara, P. et al. Automatic fiber bundle segmentation in massive tractography datasets using a multi-subject bundle atlas. *Neuroimage* **61**, 1083-1099 (2012).

26. Thiebaut de Schotten, M. et al. Atlasing location, asymmetry and inter-subject variability of white matter tracts in the human brain with MR diffusion tractography. *Neuroimage* **54**, 49-59 (2011).

27. Catani, M., Howard, R.J., Pajevic, S. & Jones, D.K. Virtual in vivo interactive dissection of white matter fasciculi in the human brain. *Neuroimage* **17**, 77-94 (2002).

28. Basser, P.J., Mattiello, J. & LeBihan, D. Estimation of the effective self-diffusion tensor from the NMR spin echo. *J Magn Reson B* **103**, 247-254 (1994).

29. Tournier, J.D., Mori, S. & Leemans, A. Diffusion tensor imaging and beyond. *Magn Reson Med* **65**, 1532-1556 (2011).

30. Jbabdi, S. & Johansen-Berg, H. Tractography: Where Do We Go from Here? . *Brain Connectivity* **1**, 169-183 (2011).

31. Ashburner, J. & Friston, K.J. Nonlinear spatial normalization using basis functions. *Hum Brain Mapp* **7**, 254-266 (1999).

32. Yeh, F.C., Verstynen, T.D., Wang, Y., Fernandez-Miranda, J.C. & Tseng, W.Y. Deterministic diffusion fiber tracking improved by quantitative anisotropy. *PLoS ONE* **8**, e80713 (2013).
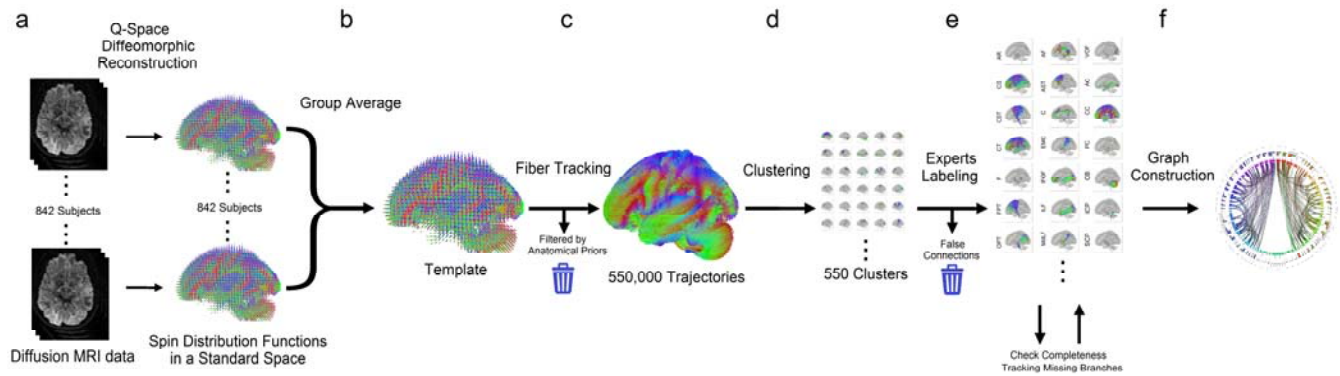
Fig. 1 Flow chart of the processing steps used to construct a population-based structural connectome of the human brain. (a) A total of 842 subjects' diffusion MRI data were reconstructed in a common standard space to calculate the spin distribution function at each imaging voxel. (b) The spin distribution functions were averaged to build a template of the diffusion characteristics of the normal population. (c) The template was used to guide a fiber tracking algorithm and generate a total of 550,000 trajectories. (d) Automatic track clustering was applied to cluster trajectories into fiber bundles. (e) A team of experienced neuroanatomists manually labeled each cluster and identified false pathways according to the neuroanatomy evidence. The clusters with the same labeled were grouped together as an atlas of structural connectome. An additional quality check was conducted to ensure complete coverage. (f) The atlas was then used to build the connectogram showing the connections between brain regions.
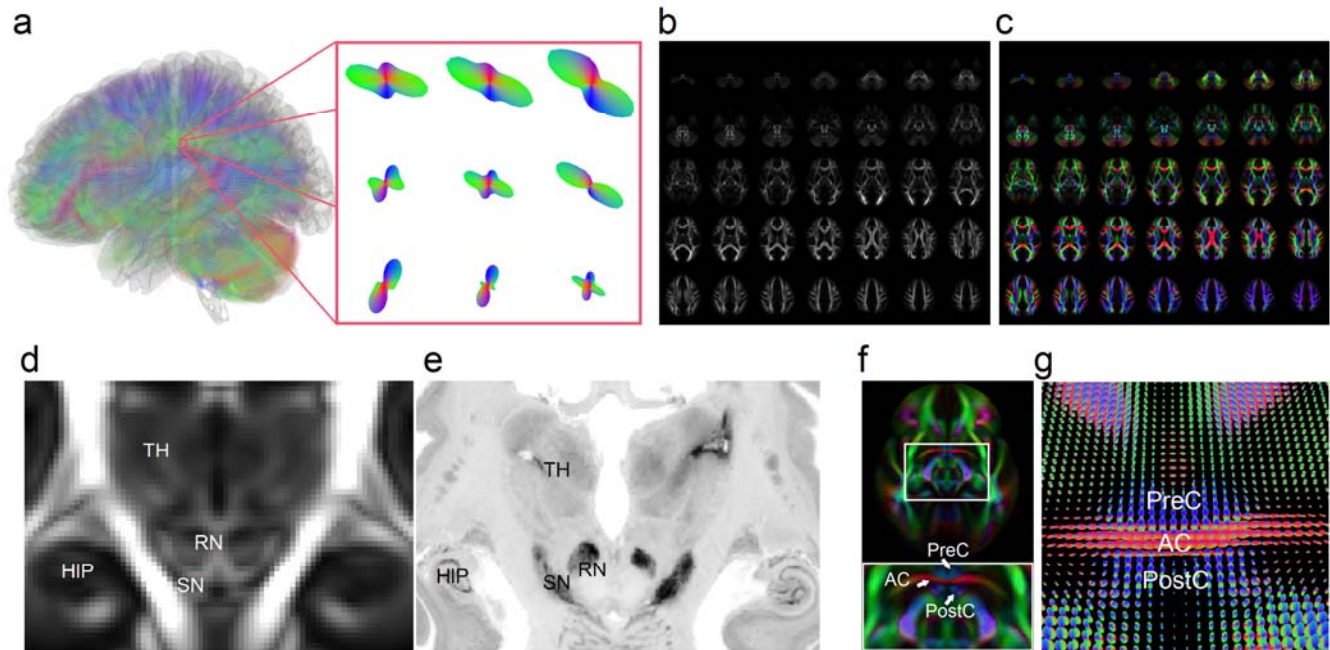
Fig. 2 (a) Diffusion MRI allows for quantifying, for each imaging voxel, the orientation distribution of the water diffusion (termed spin distribution function, SDF) to reveal the underlying structural characteristics of axonal fiber bundles in a color-coded surface (red-blue-green indicates the orientation at the x-y-z axis, respectively). The protruding points of the SDFs indicate the orientation of fiber bundles. (b)(c) The SDFs averaged from a total 842 subjects provide both magnitude (b) and orientation (c) of the local axonal connections. The information can be used to drive a fiber tracking algorithm to delineate white matter connections. (d) The SDF template of the human brain averaged from 842 diffusion MRI scans (termed the HCP-842 template) shows structural characteristics of the human brain. The magnitude map of the HCP-842 template reveals structures such as hippocampus (HIP), thalamus (TH), red nucleus (RN), and substantia nigra (SN), which are consistent with the histology image from BigBrain slides (e).

(f) The orientation map of the HCP-842 template allows for delineating the complicated structures, such

as the clamping structure between the anterior commissures (AC) and the pre-commissural (PreC) and

post-commissural (PostC) branches of the fornix. The structural characteristics are also illustrated by the

SDFs of the HCP-842 template in (g).
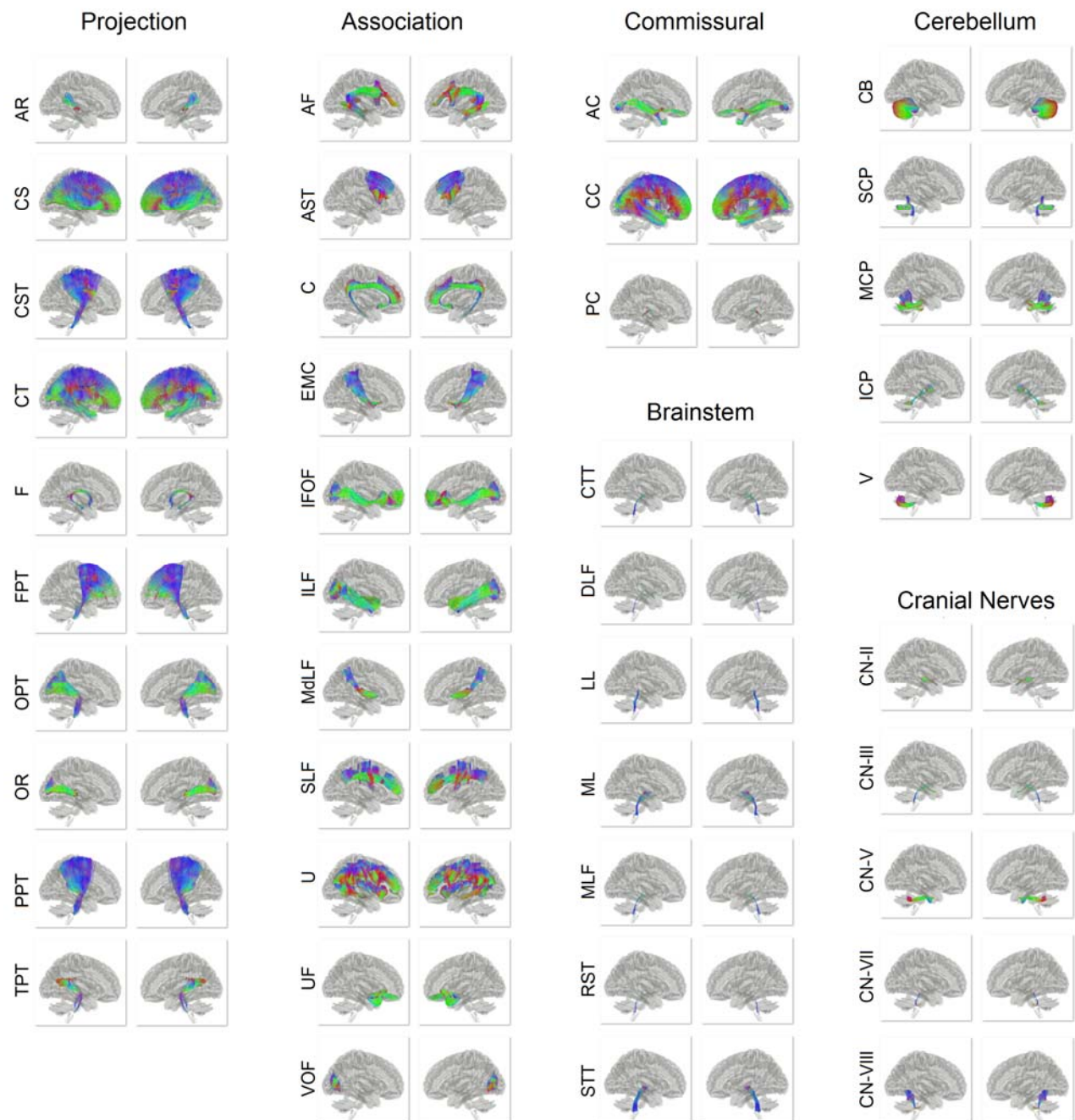
Fig. 3 Overview of the population-averaged structural connectome atlas categorized into the projection,

association, and commissural pathways in addition to cerebellum pathways, brainstem pathways, and

cranial nerves. Each pathway contains thousands of trajectories showing the representative connections

of the 842 subjects between brain regions in a standard space. The trajectories are color-coded by the

local orientation (red: left-right, green: anterior-posterior, blue: inferior-superior). This connectome atlas

provides normative connection routes between brain regions that can facilitate network analysis,

simulation and modeling.
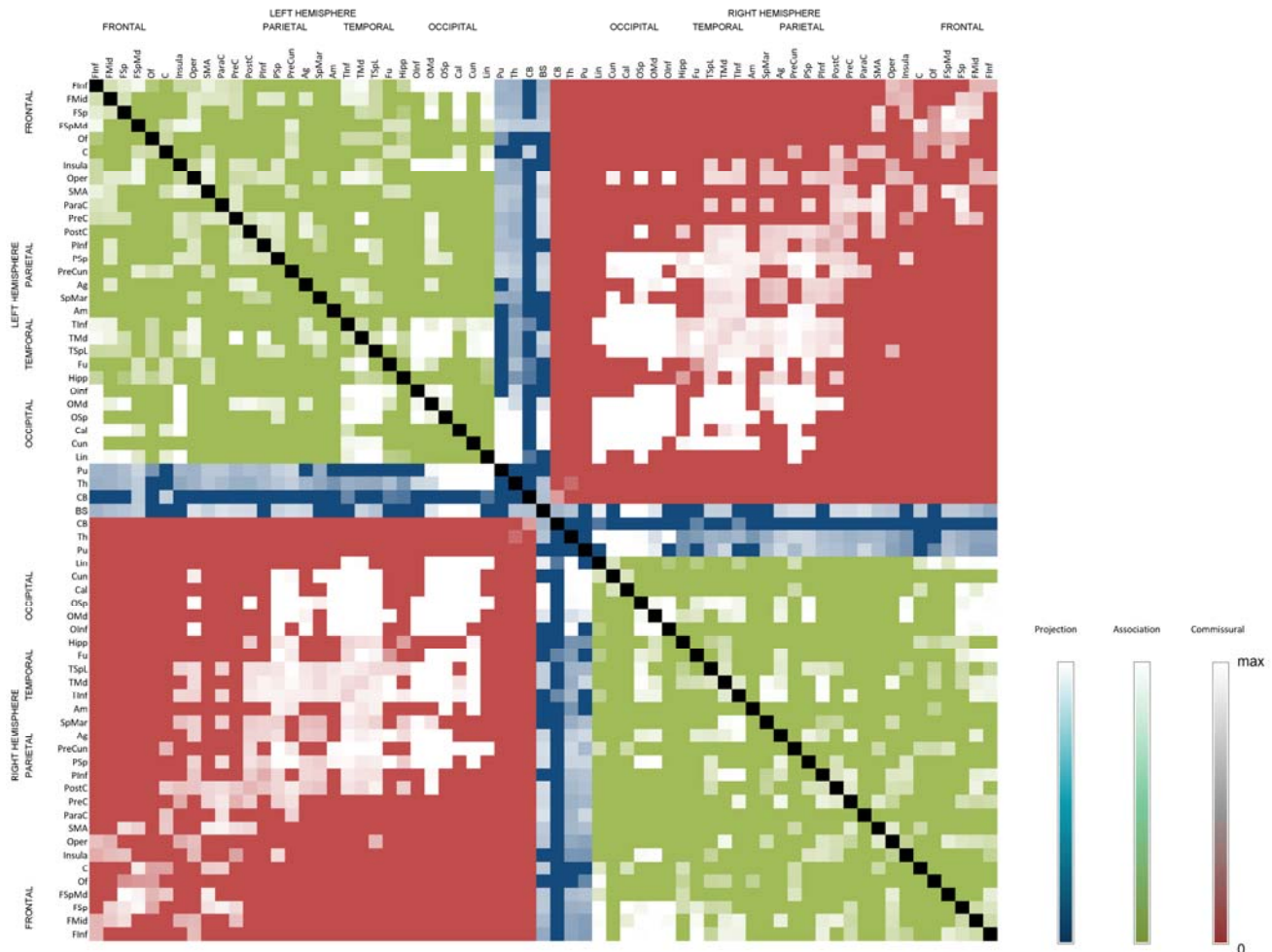
Fig. 4 The connectivity matrix constructed from the human connectome atlas. The color division shows the division of three major track systems—projection (blue), association (green), and commissural (red)—in the human brain. The intensity shows the between region connectivity quantified the magnitude of the along-track diffusion properties quantified by spin distribution functions.
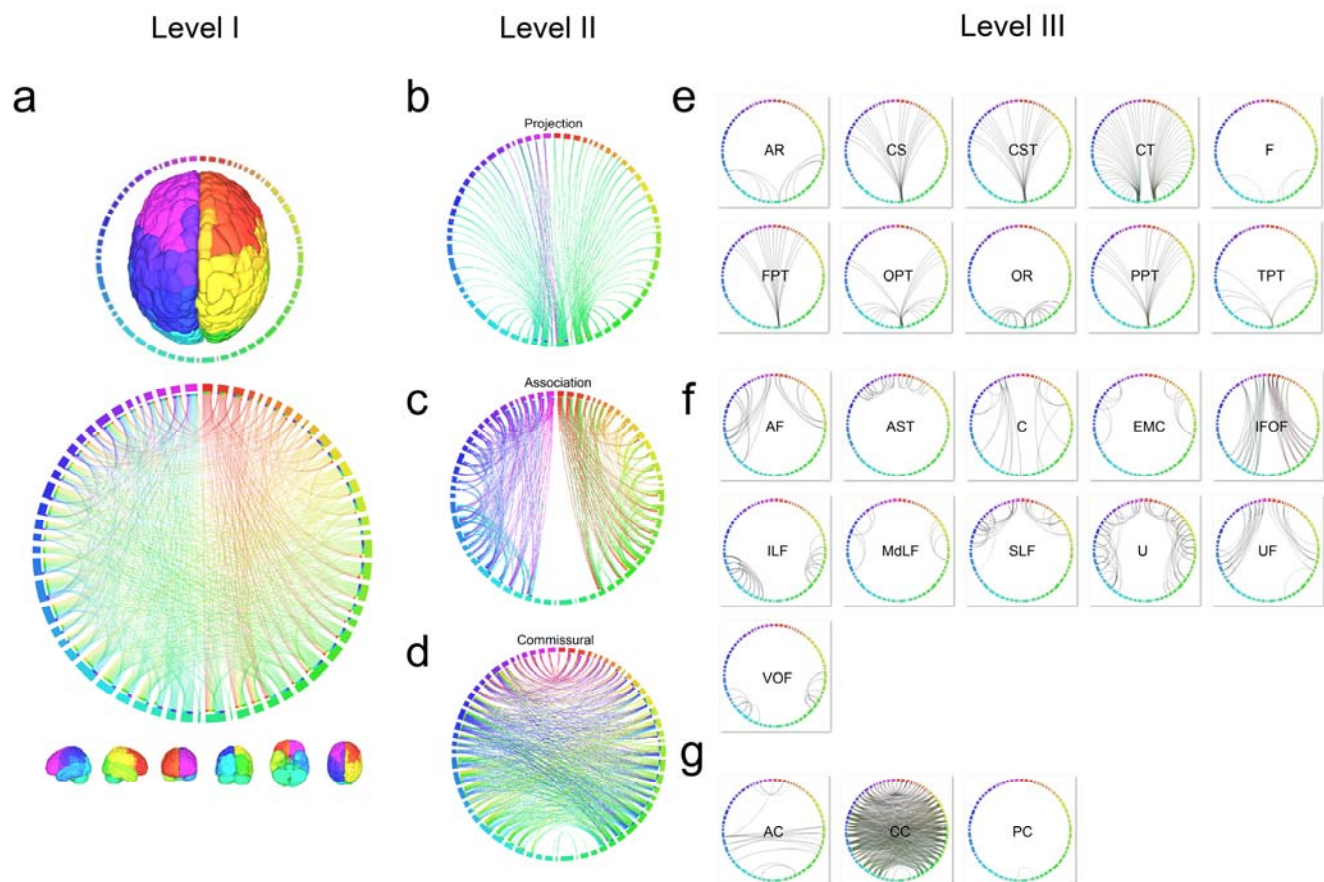
Fig. 5 The multi-level connectograms of the human structural connectome. (a) The first level of the

overall structural connectome shows a dense connections pattern in the average structure connectome.

(b) The second level of the connectogram shows the network characteristics in each pathway system.

The projection pathway forms a hub structure at thalamus, putamen, and brainstem. The association

pathway is constituted of numerous clusters in the brain networks. The commissural pathway has

long-range connections between hemispheres that provide global efficiency. (c) The third level of the

connectogram reveals the network pattern of each fiber pathways under the projection, association, and

commissural system. The connection patterns inherit the characteristics of their belonging pathway

system shown in the second level connectogram.
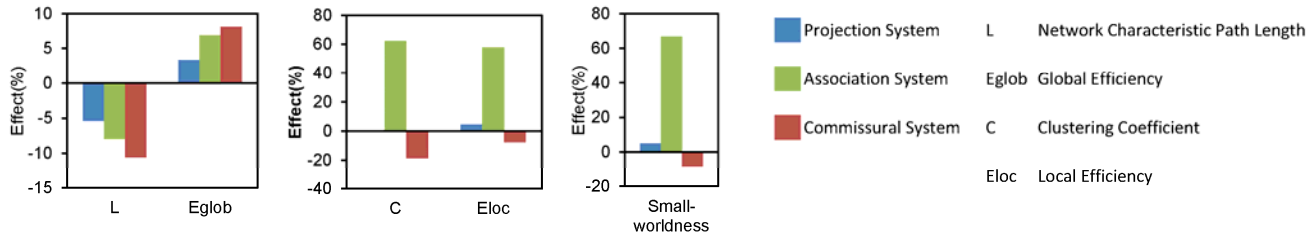
Fig. 6 The effect of the projection, association, and commissural pathways on different network measures. The percentage difference is calculated using a lesion analysis to contrast the change of the network measure after removing a set of fiber pathways. The clustering coefficient is mostly contributed by association pathways, whereas commissural pathways offer global efficiency and reduce network characteristics path length.

SUPPLEMENTARY MATERIALS
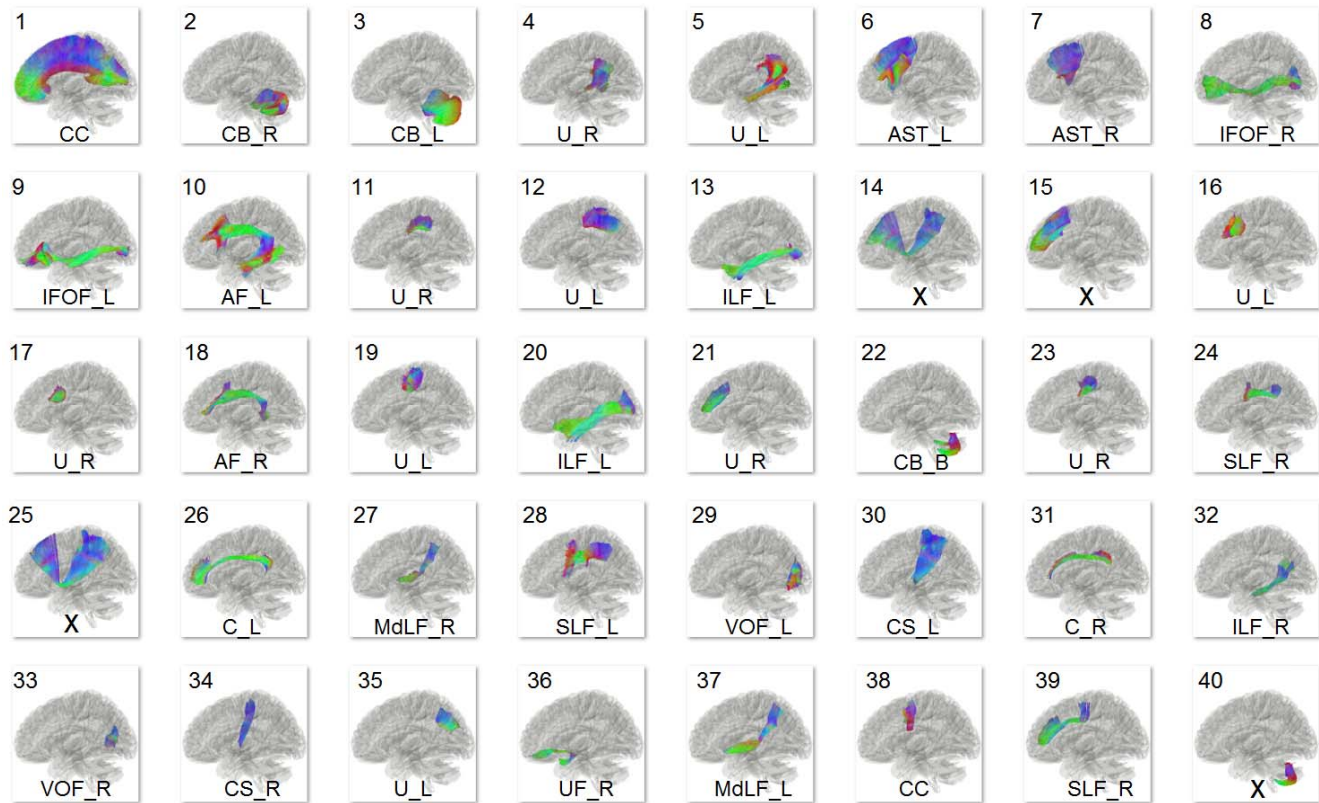
Fig. S1 The 40 largest clusters (selected from a total of 550 clusters) generated from automatic track clustering and their labels assigned by neuroanatomists. False connections are assigned by "X", whereas the others assigned by their corresponding neuroanatomy abbreviations.
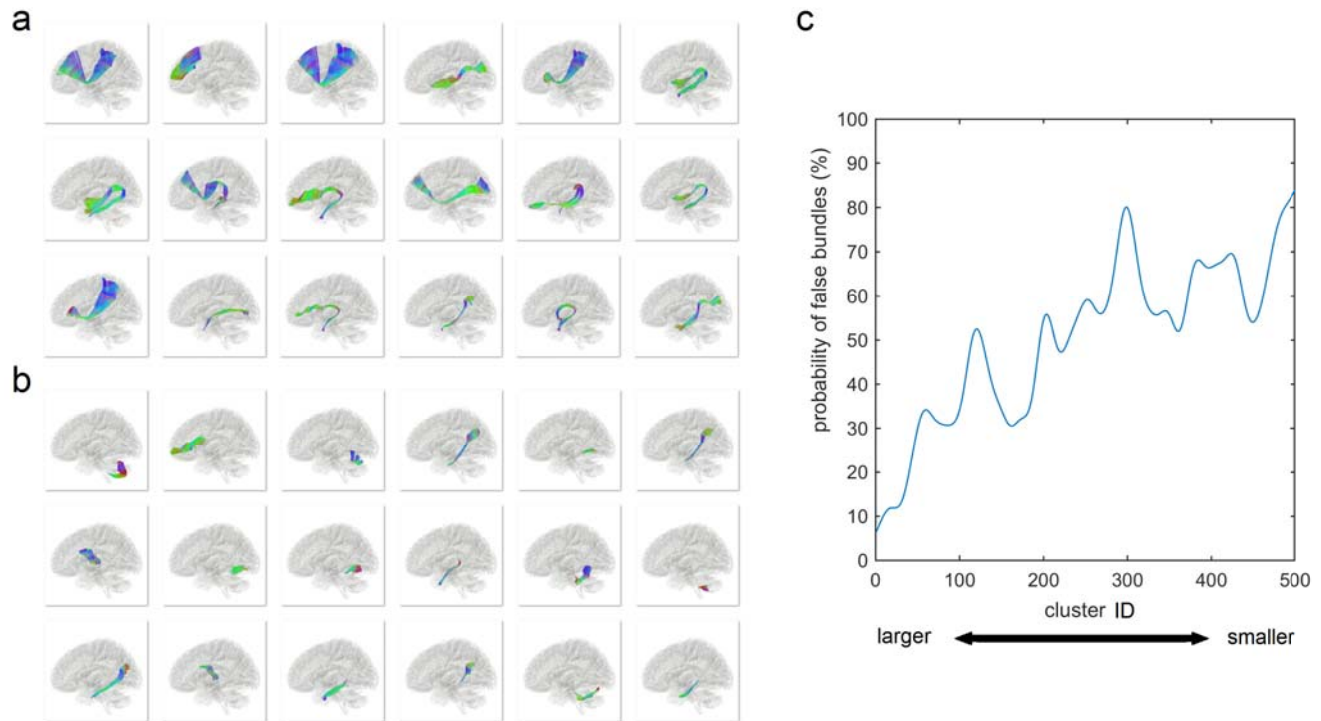
Fig. S2 False connections due to (a) false continuation and (b) premature termination identified by the neuroanatomists. A false continuation is a common cause of false trajectories and often found in regions with two fiber population cross on top of each other. Premature termination is often due to a failure in resolving crossing or branching pattern in the white matter. (c) The probability of a cluster labeled as "false" increases substantially with decreased cluster size. This suggests we can discard smaller clusters as there are mostly false connections.
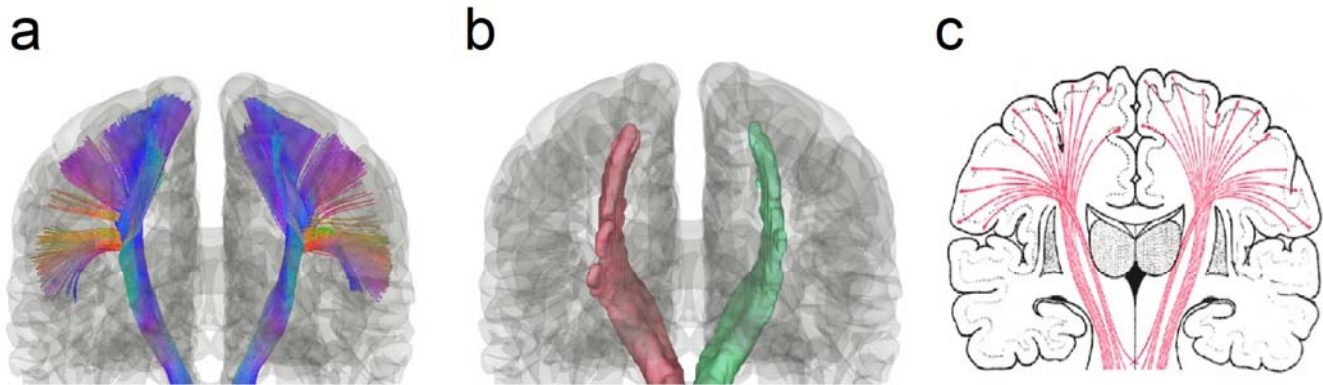
Fig. S3 The angular resolution of the structure connectome atlas illustrated. (a) The corticospinal tracks in the structure connectome atlas present a fanning pattern consistent with the known neuroanatomy presentation. (b) voxel-based white matter atlas fails to present the fanning pattern due to the limitation of its image acquisition scheme. (c) Corticospinal tracks have a fanning pattern projecting from the motor cortex, as shown in the early neuroanatomy literature.
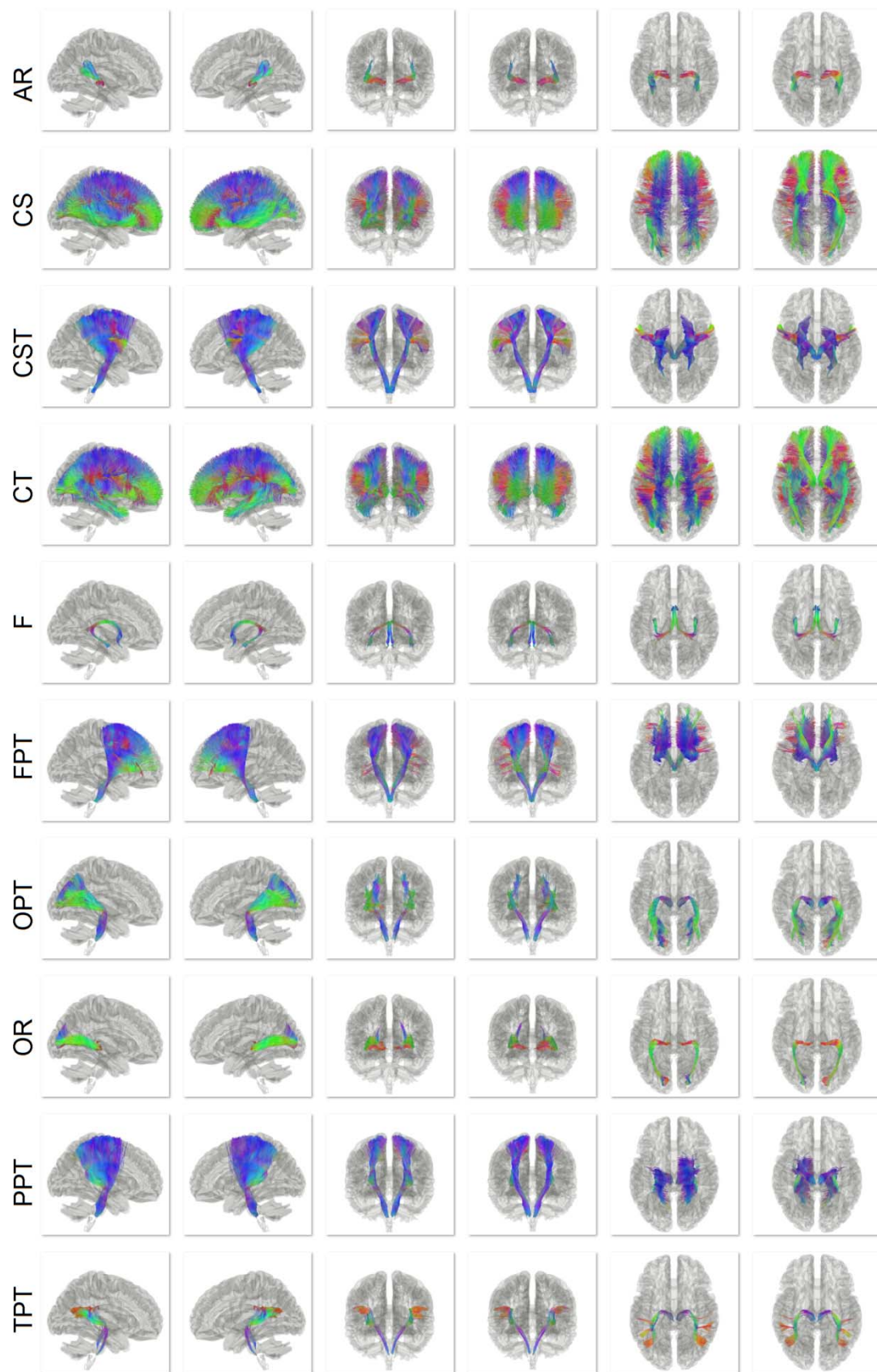
Fig. S4 The fiber bundles in the projection pathways, including acoustic radiation (AR), corticostriatal

pathway (CS), corticospinal tract (CST), corticothalamic pathway (CT), fornix (F), frontopontine

tract(FPT), occipitopontine tract (OPT), optic radiation (OR), parietopontine tract (PPT), and
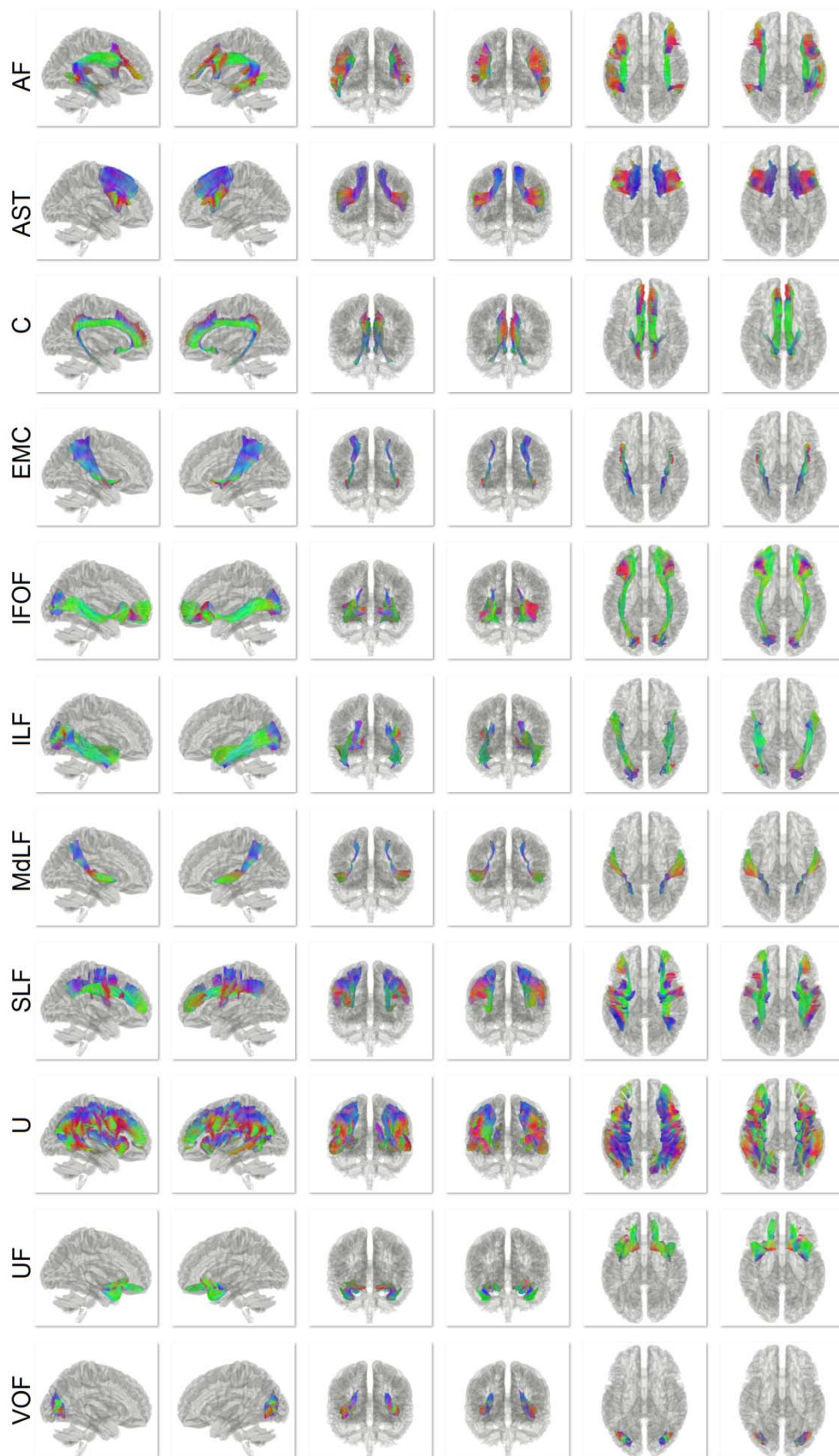
temporopontine tract (TPT).

Fig. S5 The fiber bundles in the association pathways, including arcuate fasciculus (AF), frontal aslant tract (AST), cingulum (C), extreme Capsule (EMC), inferior fronto occipital fasciculus (IFOF), inferior longitudinal fasciculus (ILF), middle longitudinal fasciculus (MdLF), superior longitudinal fasciculus (SLF), U-fibers (U), uncinate fasciculus (UF), and vertical occipital fasciculus (VOF).
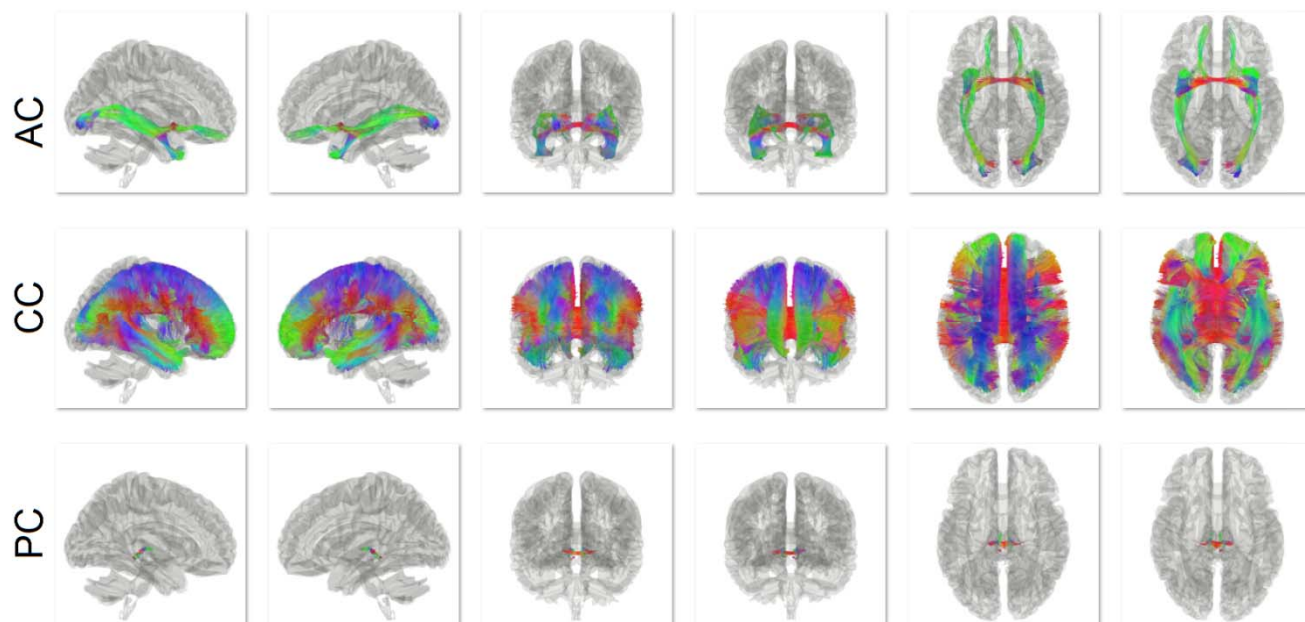
Fig. S6 The fiber bundles in the commissural pathways, including the anterior commissure (AC), corpus callosum (CC), and posterior commissure (PC).
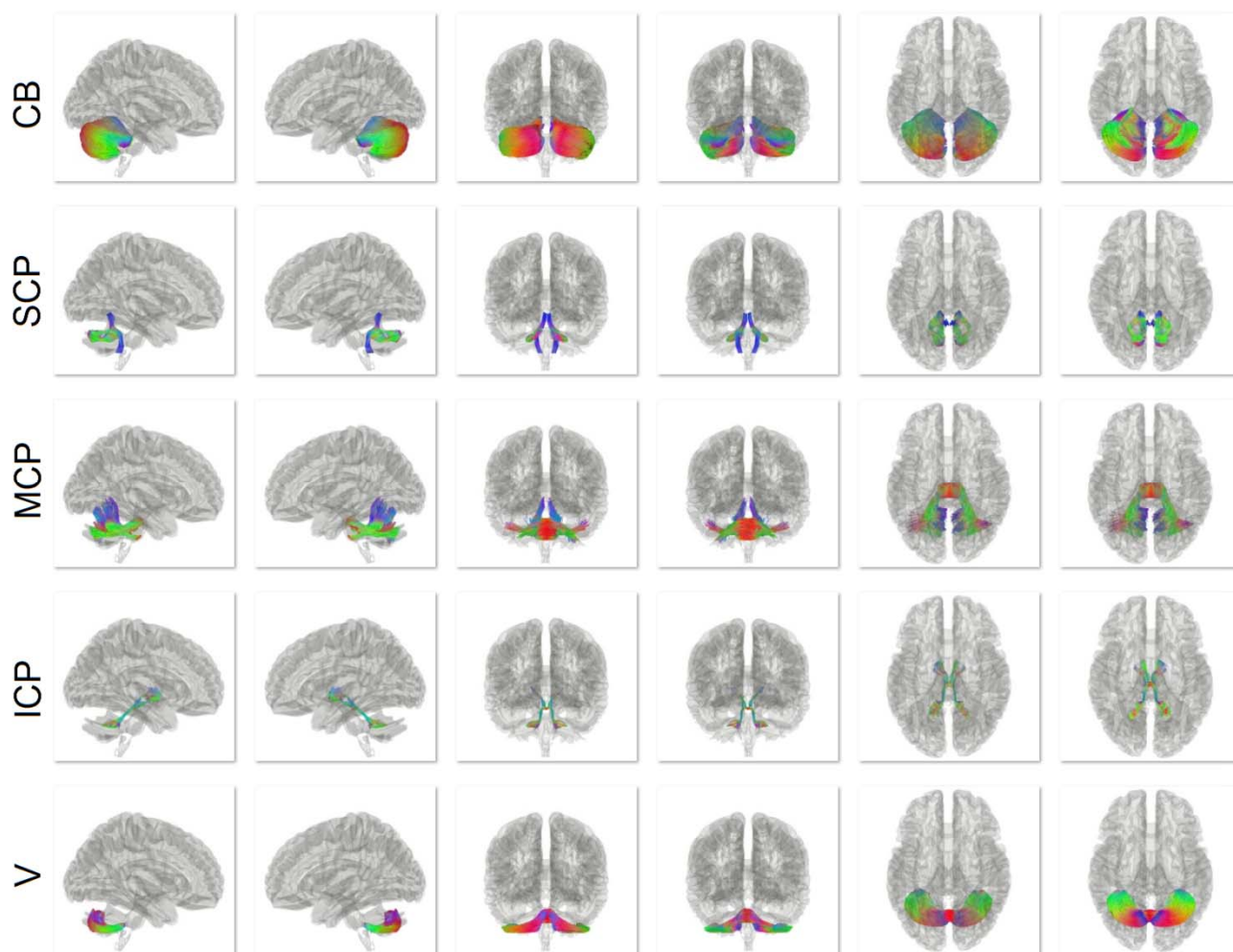
Fig. S7 The fiber bundles in the cerebellar pathways, including the cerebellum (CB), superior Cerebellar

Peduncle (SCP), middle cerebellar peduncle (MCP), inferior cerebellar peduncle (ICP), and vermis (V)
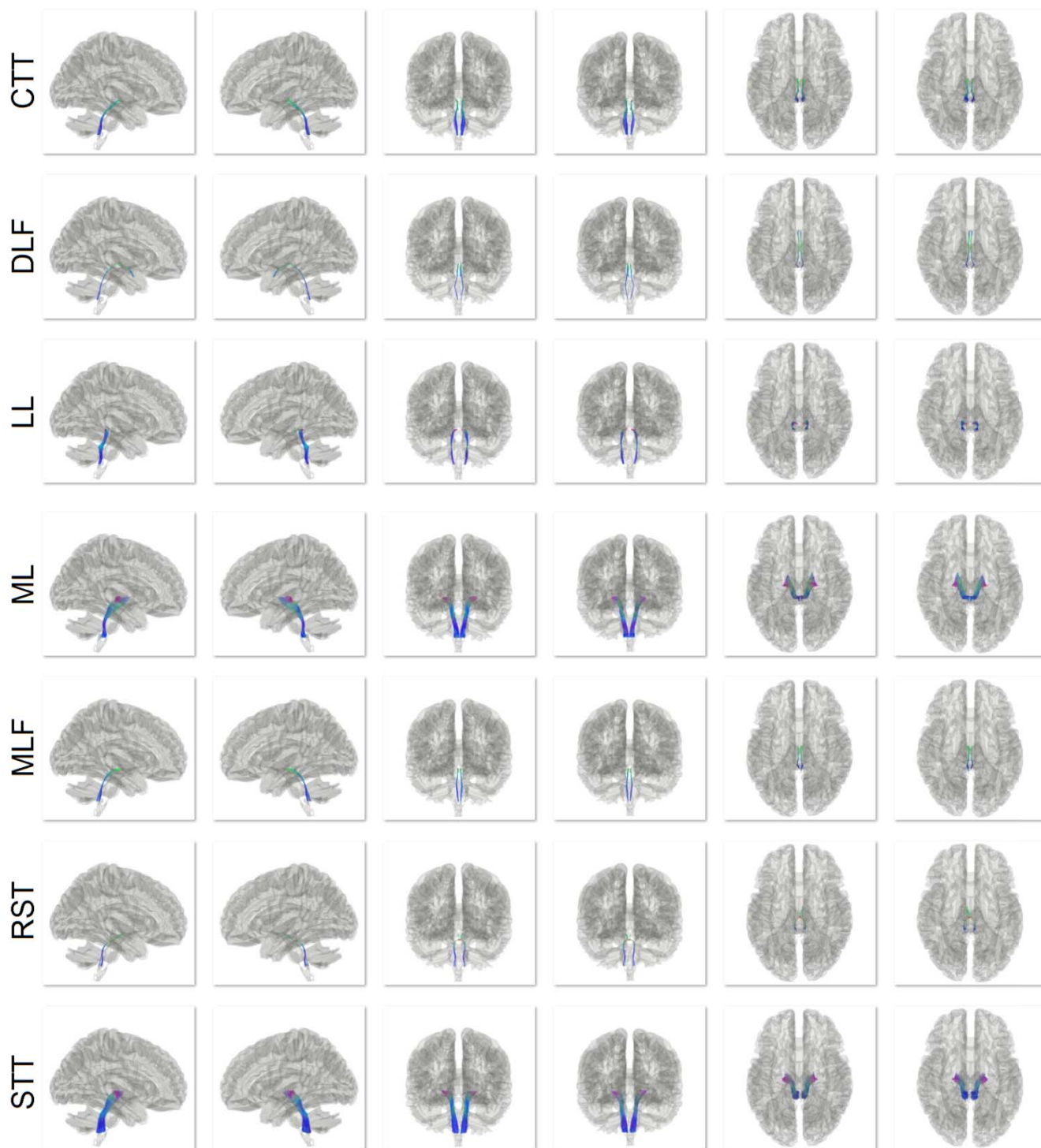
Fig. S8 The fiber bundles in the brainstem, including central tegmental tract (CTT), dorsal longitudinal

fasciculus (DLF), lateral lemniscus (LL), medial lemniscus (ML), medial longitudinal fasciculus (MLF),

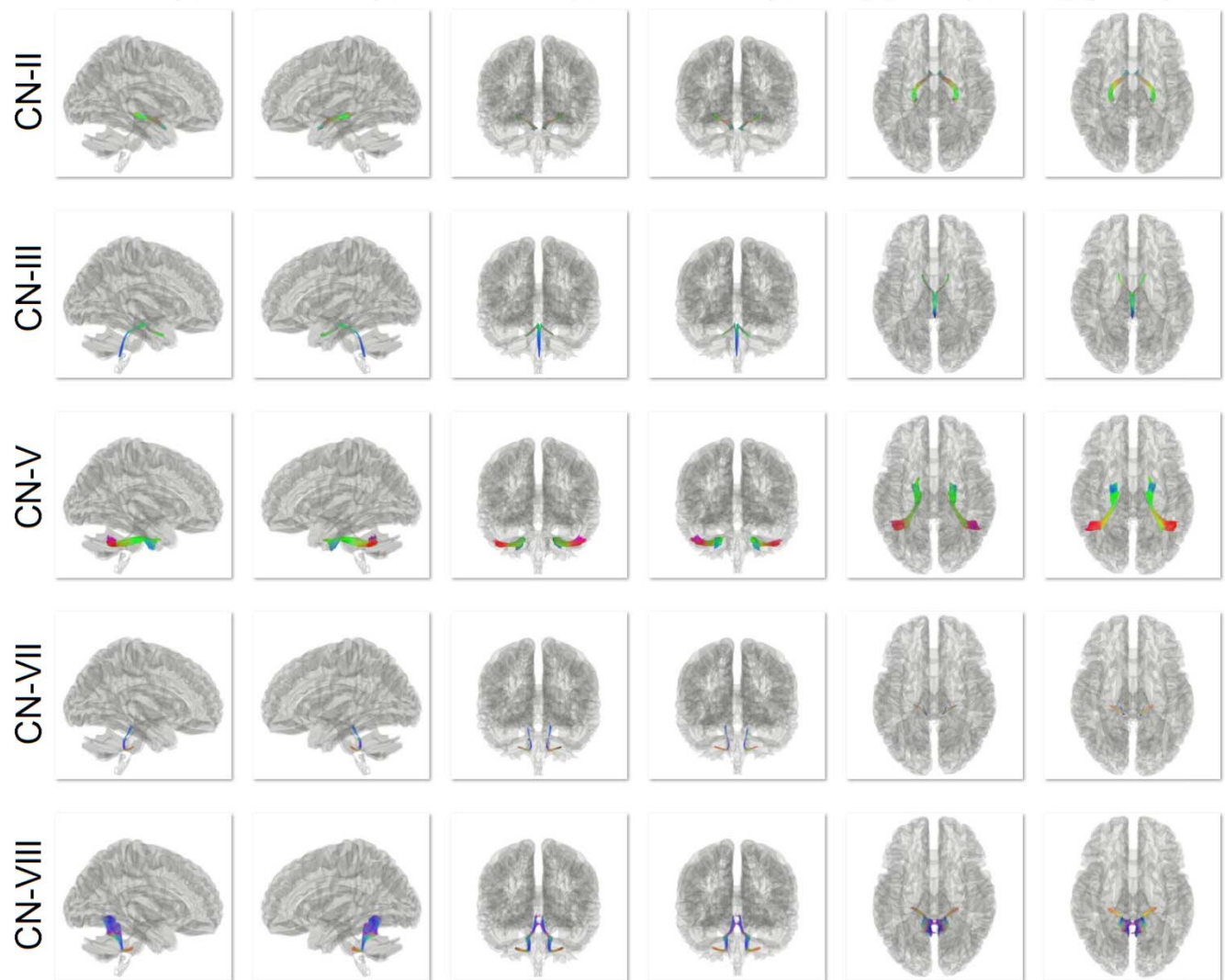rubrospinal tract (RST), and spinothalamic tract (STT).

Fig. S9 The cranial nerves included in the atlas, including the visual nerve (CN II), oculomotor (CN III),

trigeminal nerve (CN V), facial nerve (CN VII), and auditory nerve (CN VIII).
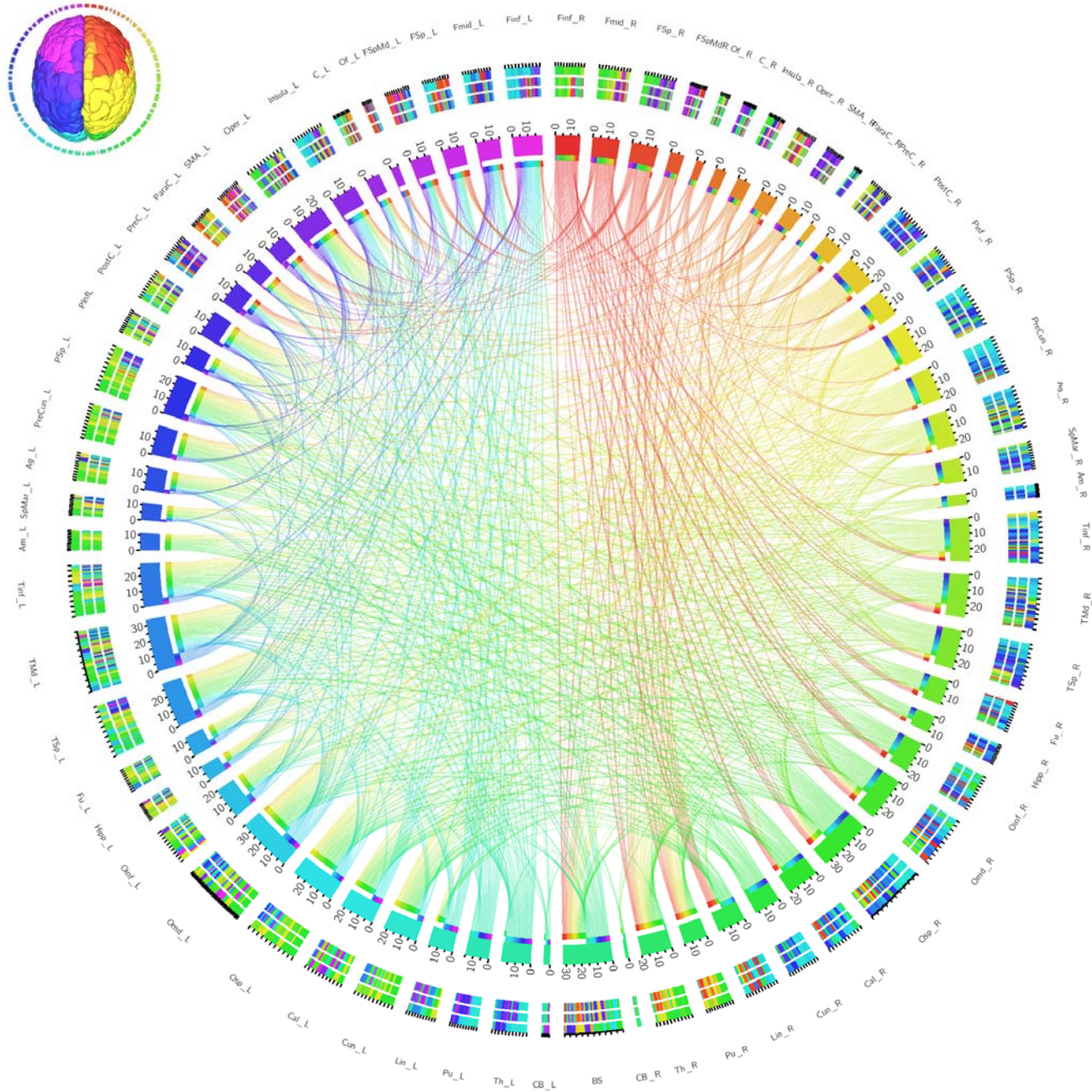
Fig. S10 The first level connectogram of the entire human brain connections. The brain is parcellation

into regions, and each region is color-coded as shown in the inset figure to the left upper corner. The left

side of the connectogram corresponds to the left hemisphere, whereas the right side of the

connectogram corresponds to the right hemisphere. The connectogram of the human brain shows a

dense network topology between the brain regions, forming a complicated architecture.
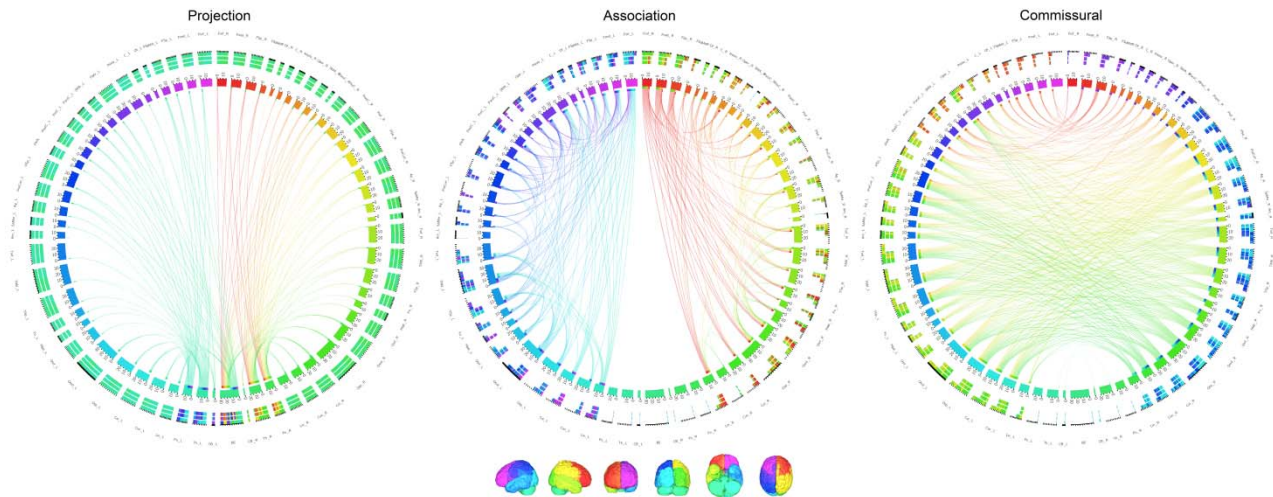
Fig. S11 The second level connectograms of the projection, association, and commissural pathways

showing the network topology of each pathway system. The projection pathway forms a hub structure in

thalamus, putamen, and brainstem. The association pathway forms numerous clusters within each

hemisphere. The commissural pathway provides long ranged communication between the two

hemispheres.

Table S1 Abbreviations of the fiber pathways

Projection Pathways

Acoustic Radiation (AR)

Corticospinal Tract (CST)

Corticostriatal Pathway (CS)

Corticothalamic Pathway (CT)

Fornix (F)

Optic Radiation (OR)

Frontopontine Tract(FPT)

Occipitopontine Tract (OPT)

Parietopontine Tract (PPT)

Temporopontine Tract (TPT)

Association Pathways

Arcuate Fasciculus (AF)

Frontal Aslant Tract (AST)

Cingulum (C)

Extreme Capsule (EMC)

Inferior Fronto Occipital Fasciculus (IFOF)

Inferior Longitudinal Fasciculus (ILF)

Middle Longitudinal Fasciculus (MdLF)

Superior Longitudinal Fasciculus (SLF)

U-fiber (U)

Uncinate Fasciculus (UF)

Vertical Occipital Fasciculus (VOF)

Commissural Pathways

Anterior Commissure (AC)

Corpus Callosum (CC)

Posterior Commissure (PC)

Cerebellum

Cerebellum (CB)

Superior Cerebellar Peduncle (SCP)

Middle Cerebellar Peduncle (MCP)

Inferior Cerebellar Peduncle (ICP)

Vermis (V)

Brainstem

Central Tegmental Tract (CTT)

Dorsal Longitudinal Fasciculus (DLF)

Lateral Lemniscus (LL)

Medial Lemniscus (ML)

Medial Longitudinal Fasciculus (MLF)

Rubrospinal Tract (RST)

Spinothalamic Tract (STT)

Cranial Nerves

Table S2	Abbreviations of the brain regions
Finf_L	Frontal Inferior Left
Fmid_L	Frontal Middle Left
FSp_L	Frontal Superior Left
FSpMd_L	Frontal Superior Medial Left
Of_L	Olfactory Left
C_L	Cingulum Left
Insula_L	Insula Left
Oper_L	Oper Left
SMA_L	Supp Motor Area Left
ParaC_L	Paracentral Left
PreC_L	Precentral Left
PostC_L	Postcentral Left
PInfL	Parietal Inferior Left
PSp_L	Parietal Superior Left
PreCun_L	Precuneus Left
Ag_L	Angular Left
SpMar_L	SupraMarginal Left
Am_L	Amygdala Left
Tinf_L	Temporal Inferior Left
TMd_L	Temporal Middle Left
TSp_L	Temporal Superior Left
Fu_L	Fusiform Left
Hipp_L	Hippocampus Left
Oinf_L	Occipital Inferior Left
Omd_L	Occipital Middle Left
Osp_L	Occipital Superior Left
Cal_L	Calcarine Left
Cun_L	Cuneus Left
Lin_L	Lingual Left
Pu_L	Putamen Left
Th_L	Thalamus Left
CB_L	Cerebelum Left
BS	BrainStem
CB_R	Cerebelum Right

Th_R	Thalamus Right
Pu_R	Putamen Right
Lin_R	Lingual Right
Cun_R	Cuneus Right
Cal_R	Calcarine Right
Osp_R	Occipital Superior Right
Omd_R	Occipital Middle Right
Oinf_R	Occipital Inferior Right
Hipp_R	Hippocampus Right
Fu_R	Fusiform Right
TSp_R	Temporal Superior Right
TMd_R	Temporal Middle Right
Tinf_R	Temporal Inferior Right
Am_R	Amygdala Right
SpMar_R	SupraMarginal Right
Ag_R	Angular Right
PreCun_R	Precuneus Right
PSp_R	Parietal Superior Right
Pinf_R	Parietal Inferior Right
PostC_R	Postcentral Right
PreC_R	Precentral Right
ParaC_R	Paracentral Right
SMA_R	Supp Motor Area Right
Oper_R	Oper Right
Insula_R	Insula Right
C_R	Cingulum Right
Of_R	Olfactory Right
FSpMdR	Frontal Superior_Medial Right
FSp_R	Frontal Superior Right
Fmid_R	Frontal Middle Right
Finf_R	Frontal Inferior Right